Broadband enhancement of mid-wave infrared absorption in a multi resonant nanocrystal-based device

Tung Huu Dang, Claire Abadie, Adrien Khalili, Charlie Gréboval, Huichen Zhang, Yoann Prado, Xiang Zhen Xu, Djamal Gacemi, Armel Descamps-mandine, Sandrine Ithurria, et al.

Broadband enhancement of mid-wave infrared absorption in a multi resonant nanocrystal-based device

Tung Huu Dang[1,2], Claire Abadie[2,3], Adrien Khalili[2], Charlie Gréboval[2], Huichen Zhang[2], Yoann Prado[2], Xiang Zhen Xu[4], Djamal Gacemi[1], Armel Descamps- Mandine[5], Sandrine Ithurria[4], Yanko Todorov[1], Carlo Sirtori[1], Angela Vasanelli[1*], Emmanuel Lhuillier[2*]

[1] Laboratoire de physique de l'Ecole Normale Supérieure, ENS, Université PSL, CNRS, Sorbonne Université, Université de Paris, 75005 Paris, France
[2] Sorbonne Université, CNRS, Institut des NanoSciences de Paris, INSP, 75005 Paris, France.
[3] ONERA - The French Aerospace Lab, 6, chemin de la Vauve aux Granges, BP 80100, 91123 Palaiseau, France.
[4] Laboratoire de Physique et d'Etude des Matériaux, ESPCI-Paris, PSL Research University, Sorbonne Université Univ Paris 06, CNRS UMR 8213, 10 rue Vauquelin 75005 Paris, France.
[5]Centre de MicroCaractérisation Raimond Castaing, ECA, 3 rue Caroline Aigle, 31400 Toulouse, France

Abstract: Light management is one of the main challenges to address when designing a sensor from a nanocrystal (NC) array. Indeed, the carrier diffusion length, limited by hopping mechanism, is much shorter than the absorption depth. Several types of resonators (plasmon, Bragg mirror, guided mode, Fabry-Perot cavity) have been proposed to reduce the volume where light is absorbed. All of them are inherently narrow bands, while imaging applications focus on broadband sensing. Here, we propose an infrared sensor in the short and mid-wave infrared (SWIR and MWIR) that combines three different photonic modes to achieve broadband enhancement of the light absorption. Moreover, we show that these three modes can be obtained from a simple structure where the NC film is coupled only to a grating and a top metallic layer. The obtained device achieves a high responsivity of >700 $mA.W^{-1}$, a detectivity up to $2x10^{10}$ Jones at 80 K, and a short response time of 11 µs.

*To whom correspondence should be sent: angela.vasanelli@ens.fr, el@insp.upmc.fr

Introduction

Thanks to their size-tunable optical features, colloidal nanocrystals (NCs) have become key building blocks[1] for optoelectronics not only as light down-converters for display but also for LEDs[2] and solar cells[3]. For a long time, the effort to improve nanocrystal integration has focused on surface chemistry[4] to enhance carrier mobility and band alignment[5,6] to optimize the photodiode design. On the other hand, light-matter coupling remains far less investigated compared to what has been studied in the case of III-V epitaxially grown devices. This is nevertheless a question of utmost importance since the absorption depth (few µm) in NC films is typically ten times longer than the carrier diffusion length (<100 nm). Thus, photonic strategies that enable to spatially distribute the incident light into nanocrystal devices must be developed.

Recently, some efforts have been made in this direction, especially in the near and mid-infrared. Incident light can be trapped in a mode propagating along the substrate either using propagative (guided-mode resonances[7–9]) or evanescent (surface plasmon polariton[5,10,11]) modes. Alternatively, a Fabry-Perot cavity[12–14] or a Bragg mirror[15] can be designed to generate a standing wave that spatially overlaps with the NC film. Consequently, it is possible to reshape the device's photocurrent spectrum and enhance the signal at a given wavelength. For a 200 nm film, absorption close to the exciton resonance at ≈2.5 µm can typically be increased from 10 % to more than 70 %[9] by inserting the NC film in a photonic structure. In general, the linewidth of the absorption resonance depends on the characteristics of the cavity. A quality factor of 180 (corresponding to a linewidth of 30 cm^{-1}) has been achieved with a Bragg mirror[15], while the quality factor of a plasmonic mode is typically in the order of 10. However, in all mentioned cases, the linewidth of the absorption resonance remains narrow compared to the one targeted for imaging applications (2000 - 5000 cm^{-1} for a central frequency of 5000 cm^{-1} or a range of more than 2 µm). Solar cells face the same issue, and broadband enhancement of the absorption, over the whole visible, has been reported by combining up to 9 different resonances[16]. This approach has already been employed for NCs in the infrared by designing a plasmonic array on the top of a Fabry-Perot[12] cavity containing a NC film. This strategy comes with the price of a more complicated fabrication process. Here, we demonstrate that up to three resonances can be obtained from a single 1D metallic grating. For this, we exploit the topological frustration characteristic of one-dimensional gratings, which display Fabry-Perot modes under the grating stripes in TM polarization and over the slit regions in TE polarization[17]. We add to these two resonances a surface plasmon mode generated at the interface between the NC and the metallic layer. By combining these resonances in the two polarizations, we demonstrate a broadband enhancement of the absorption over ≈2500 cm^{-1} (from 2 to 4 µm). The device presents a large responsivity (>700 $mA.W^{-1}$ – equivalent to ≈30% external quantum efficiency at 3 µm), a detectivity up to $2x10^{10}$ Jones at 80 K, and a short response time of 11 µs. Our strategy also reduces the dependence of the photoresponse on the polarization, which is characteristic of most devices based on 1D grating geometries.

Results and discussion

Our objective is to obtain a multi resonant structure while keeping the fabrication steps as simple as possible since NCs could easily get damaged when exposed to fabrication conditions. The strategy is to design a structure that can feature multiple roles**. Figure 1**a introduces the design of our photodetector, which contains five different layers: sapphire substrate, gold grating, NC film, PMMA layer, and a top gold mirror. The film of HgTe NCs, whose band edge is in the MWIR, is coupled to a grating and a top metallic layer to form an array of double metal cavities, allowing electromagnetic field confinement in subwavelength regions.[17,18] These photonic structures are well suited to NC

devices as they concentrate the absorption in only a few hundred nanometers above the interdigitated contacts, which is comparable to the carrier diffusion length. This is in contrast with epitaxially grown semiconductors, in which the active layer is several µm away from the metallic contact.

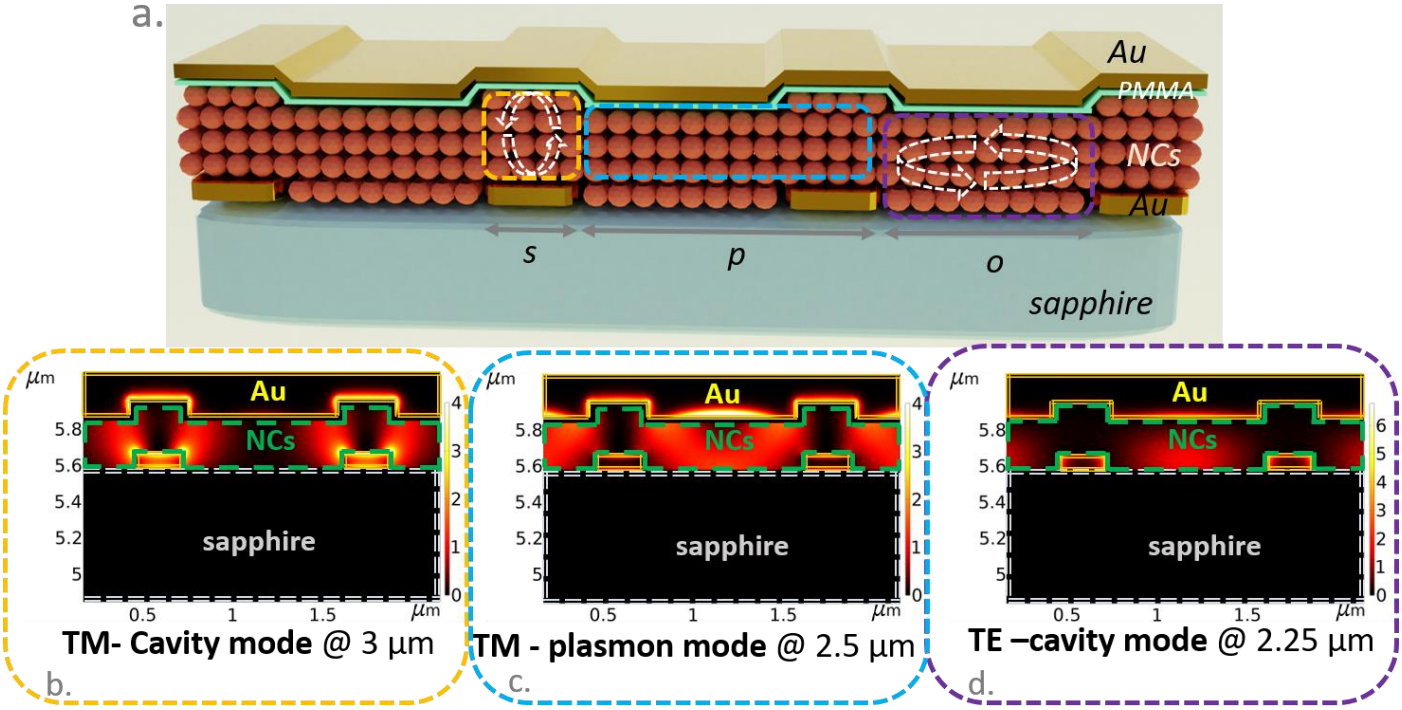

Figure 1 Multi resonant absorption design*. a. Schematic of the multi-resonant MWIR absorbing device. Arrows indicate the regions where cavities are formed due to an impedance mismatch between single and double metal regions. b. Absorption map of the device at 3 µm corresponding to the TM cavity mode resonance wavelength. c. Absorption map of the device at 2.5 µm corresponding to the TM surface plasmon mode wavelength. d. Absorption map of the device at 2.25 µm corresponding to the TE mode resonance wavelength. For parts b-d, the color scale corresponds to the absorption magnitude (in arbitrary units). Electric field maps are provided in Figure S3. All the parameters employed for electromagnetic simulations are summarized in paragraph SI 1.1.*

The optical features of the structure are determined by the geometrical parameters of the grating: the gold stripe size *s*, the grating period *p*, and the opening *o*=*p*-*s*, see **Figure 1a**. Under TM polarization, metal-dielectric-metal cavities are formed on top of the stripes due to the impedance mismatch between the double metal region and the single metal one. Their resonance wavelength is defined by the stripe size *s*. This cavity mode strongly enhances the absorption of NCs close to the stripes, see **Figure 1**b and S3a. Simultaneously, the interface between the top gold mirror and the PMMA/NC film supports a surface plasmon mode. Thanks to the periodicity of the cavity grating, diffraction phenomena appear and the surface plasmon (SP) polariton dispersion is folded back in the first Brillouin zone ($k_x = \pi/p$), as shown in the dispersion map in **Figure 3**a (red dashed line) and S6. The wavelength of the diffracted orders of the surface plasmon polariton mode is thus controlled by the period *p*. The SP mode decays in the NC film and intensifies NC absorption over extended areas between two adjacent metals, see **Figure 1**c and S3b. By carefully choosing *s* and

p, it is possible to generate two modes that are quasi matched in energy, see the dispersion map in **Figure 3**a. Here, we choose to match the cavity mode with the exciton energy, while the plasmon is slightly blue-shifted to broaden the device absorption for angles close to normal incidence. As a result, broadband absorption can be expected in TM polarization.

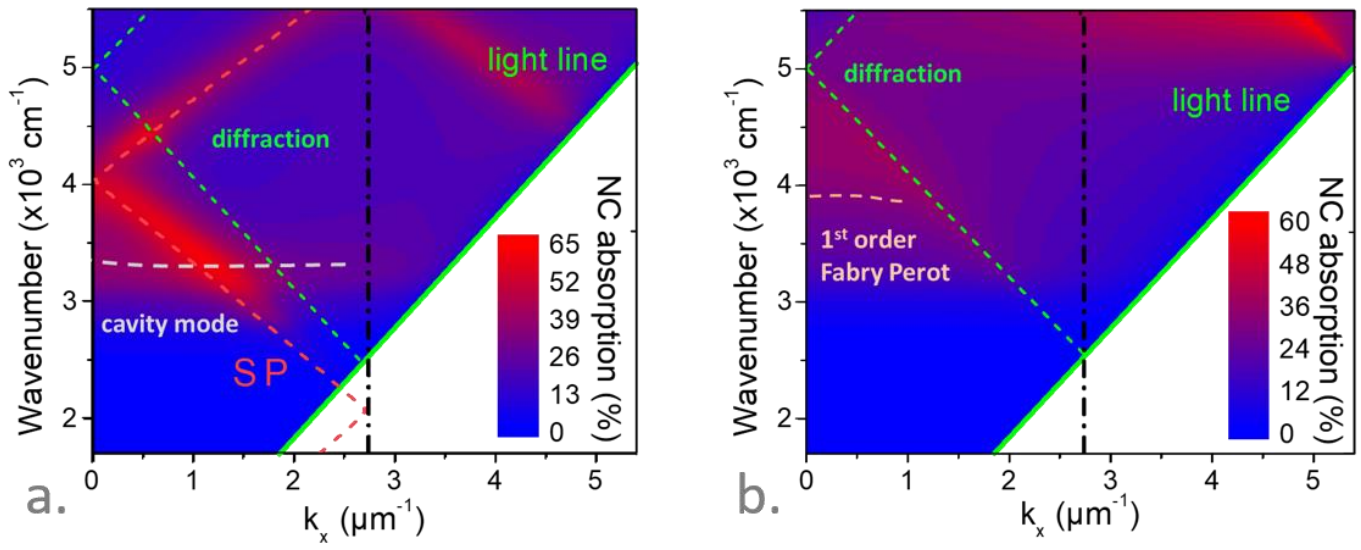

***Figure 2**. **Spectroscopic properties of a multi resonant structure** a. (resp. b) Calculated NC absorption (in color scale) as a function of the photon wavenumber and wavevector in the x direction for TM (resp. TE) polarization. All the parameters employed for electromagnetic simulations are summarized in paragraph SI 1.1. The continuous green line is the light line in the sapphire, while the green dashed lines represent its diffracted orders. The dashed red line represents the calculated SP polariton dispersion, together with its diffracted orders. The vertical black line indicates the edge of the first Brillouin zone, at $k_x = \pi/p$. The horizontal white dashed lines represent the Fabry-Perot cavity modes.*

In TE polarization, the presence of the grating allows obtaining light confinement in the slits between two stripes (see Figure S3c). This confinement is associated with Fabry-Perot modes with resonant energies driven by the opening *o* and the NC film thickness, see discussion in the supporting information paragraph 1.4. Consequently, the absorption of NCs in the openings is enhanced, see **Figure 1**d. Here, the energy of this mode is set to broaden further the device's spectral response with an absorption peak at 2.25 µm, see **Figure 3**b and S5. At large incident angles, when diffraction starts to play a significant role, the Fabry-Perot mode becomes dispersive. A second-order Fabry-Perot resonance also appears at large incidence angles around 5500 cm^{-1} (≈ 1.8 µm). As the values of *p* and *s* also set the mode wavelength in TM polarization, the Fabry-Perot resonance in TE can be tuned by varying the nanocrystal film thickness, see figure S5d.

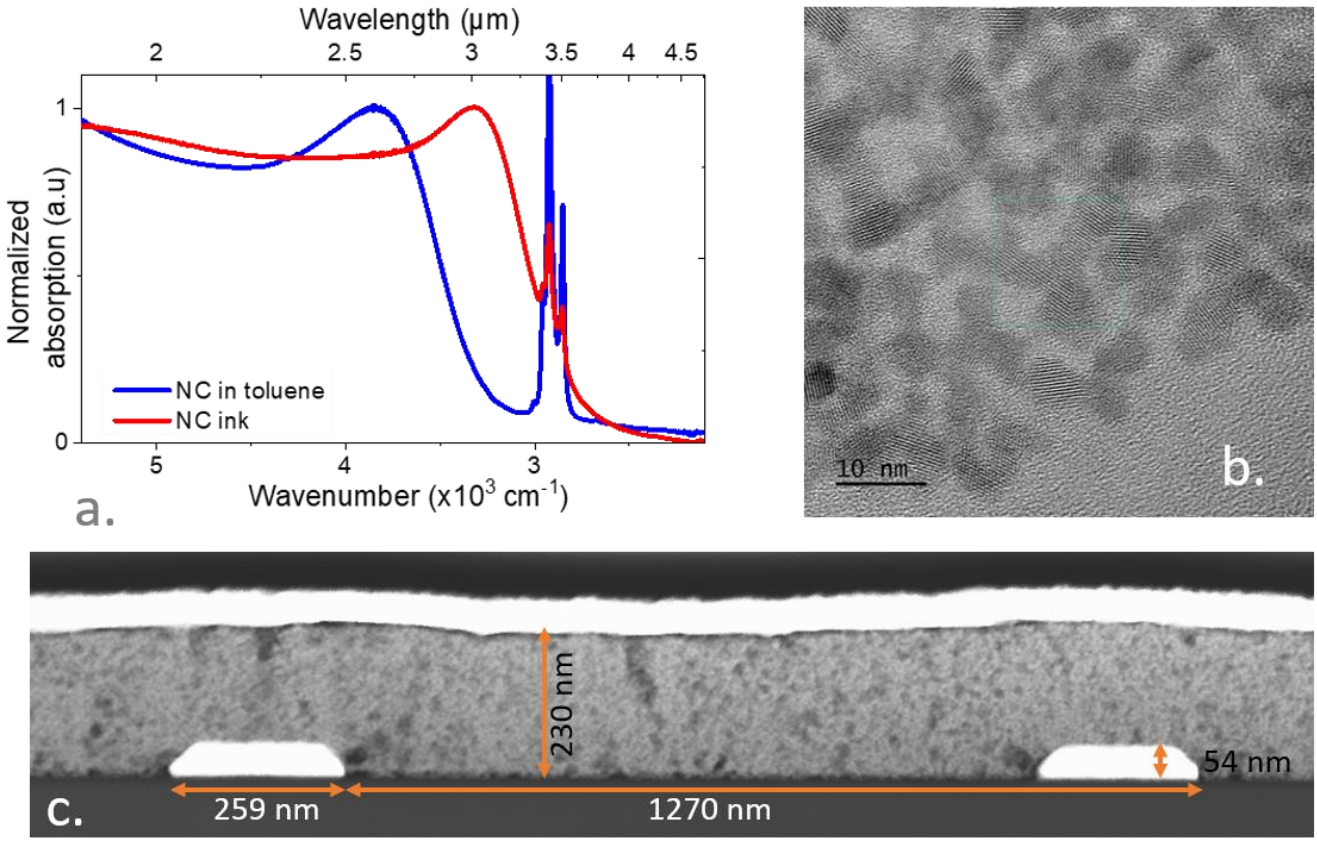

***Figure 3**. **Characterisation of the nanocrystal film and device** a. Absorption of HgTe NCs in solution (DDT capped) and under ink form ($HgCl_2$-MpOH capped). b. TEM image of the HgTe NC presenting MWIR absorption. c. TEM image of a side view of the device.*

To confirm our prediction, we fabricated the device depicted in **Figure 1**a and S1. As the sample is backside illuminated, a sapphire substrate is chosen to provide good transparency for SWIR and MWIR. On top of the substrate, we fabricated by e-beam lithography a grating (p = 1225 nm, s = 250 nm, and o = 975 nm) which plays a dual role: functioning as interdigitated electrical contacts for photoconductive operations and specifying electromagnetic field modes coupled with the NC film. A side view transmission electron microscopy image of the device is shown in **Figure 3c** and confirms that obtained geometrical parameters are close to the targeted ones.

In the following part of this article, the reported transport is a planar electrical transport between two consecutive grating periods. The electrodes are functionalized with a 250 nm thick film of HgTe NCs.[19] In order to design a MWIR absorbing device, we use HgTe NCs grown using the procedure developed by Keuleyan *et al*.[20] According to transmission electron microscopy (TEM), the obtained NCs have a tripod shape,[21] see **Figure 3**b. In solution, the particles present an excitonic peak at around 2.5 µm. The excitonic absorption shifts to above 3 µm once the particles are capped with short ligands (*i.e.*, a mixture of $HgCl_2$ and mercaptoethanol) and compatible for transport,[22–24] see **Figure 3**a. We observe that after ligand exchange, the relative weight of the peak resulting from C-H bond resonance with respect to the exciton is reduced. This is due to the removal of the free ligands and ligand length reduction. The cut-off wavelength of this ink reaches 4 µm. The NC deposition on the top of the grating appears to be conformal. This characteristic is also included in our electromagnetic modeling. Then, the NC film is covered by a thin (30 nm) insulating PMMA layer

and a top gold layer (40 nm). The PMMA layer is introduced to prevent electrical shorts, and its thickness is small compared to the plasmon decay length in the NC film. Energy dispersive X-ray spectroscopy mapping (Figure S9) of the device has been conducted and, in particular, confirms the presence of an organic layer at the interface between the HgTe NC film and the top electrode.

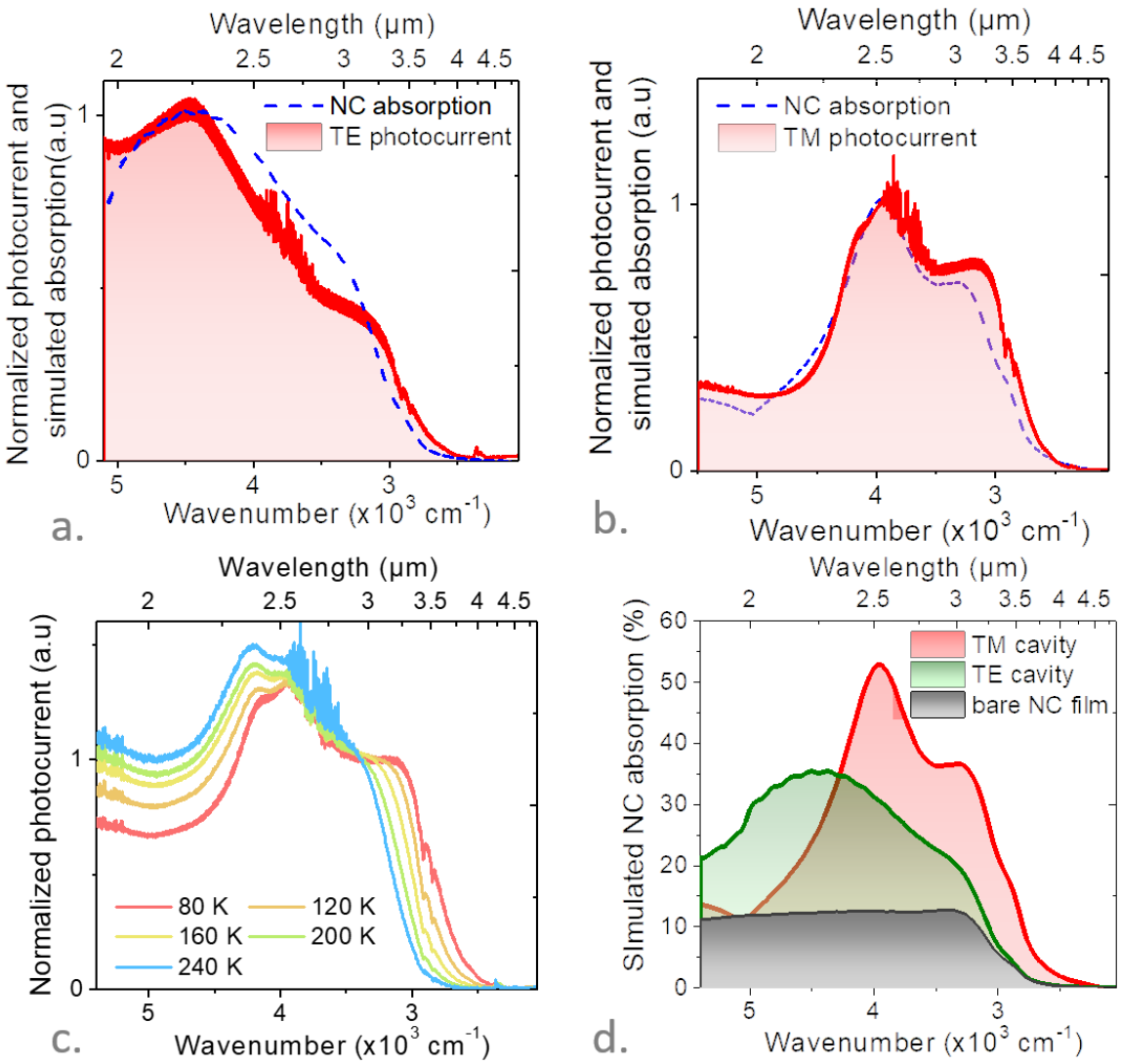

Figure 4 Broadband absorption in the short and mid-wave infrared*. a. (resp b.) Simulated NC absorption and experimental photocurrent spectra under TE (resp. TM) polarization, at 80 K. c. Experimental unpolarized photocurrent spectra at various temperatures. d Simulated absorption spectra for the bare NC film and the same film introduced in our multi-resonant geometry.*

The photocurrent spectra of the device have been measured, see figure S10. Under TE polarization (**Figure 4**a), we observe two main features. The first feature that appears around 3000 cm^{-1} (3.2 µm) is attributed to the absorption band edge of the NCs. The second noticeable feature at 4500 cm^{-1} (2.25 µm) corresponds to the Fabry-Perot resonance. For TM polarization, a doublet can be observed with a clear overlap of two absorption features, see **Figure 4**b. The bluer component around 4000 cm^{-1} (2.5 µm) is associated with the plasmon peak, while the redder component at 3000 cm^{-1} (3.2 µm) is related to the cavity mode and the excitons. Note that the photocurrent spectra nicely match the simulated absorption spectrum of the NC film (*i.e.,* excluding metal losses). The

main notable discrepancy between the photocurrent and the simulated absorption spectra is a small redshift. This relates to the redshift of the HgTe NC absorption at low temperatures since the photocurrent spectra were measured at 80 K, while the NC absorption is calculated using room temperature permittivity. This redshift can also be observed in a series of unpolarized photocurrent spectra of the device at different temperatures in **Figure 4**c. As the device is cooled down, the band edge of the device is redshifted due to an increase in the bandgap energy of HgTe NCs. Indeed, the wider bandgap induces a change in the spectral overlap of the material absorption with the different resonances. Thus, the magnitude of the absorption associated with each mode is affected, although their energies barely change since the latter are driven mainly by geometrical factors. In **Figure 4**d, we compare the absorption spectrum of a bare 250 nm NC film with the TM and TE absorption spectra of NC film coupled with our photonic structure. The simulations show a significant improvement in both TE and TM absorptions over a broad range, as confirmed by the photocurrent spectra (Figure S10).

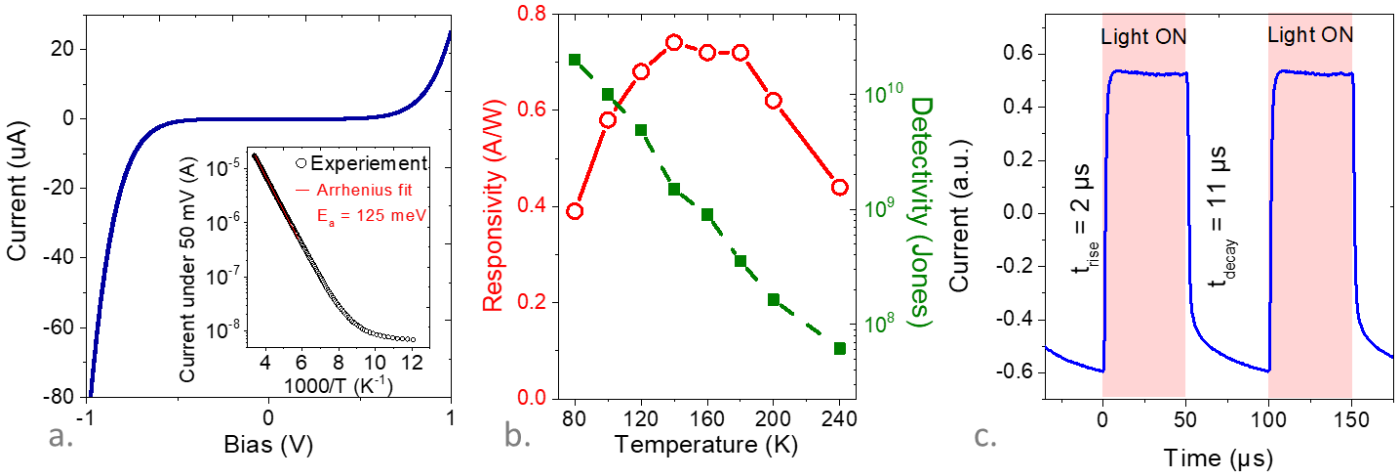

***Figure 5 Device performances**. a. IV curve of the device at 80 K. The inset is the I-T curve, whose part close to room temperature is fitted with an Arrhenius law, presenting a 125 meV activation energy. b. Responsivity (under broadband blackbody radiation operated at 980 °C) and detectivity of the device as a function of the device operating temperature when the applied bias is 0.2 V and the light is modulated at 1 kHz. c. Current as a function of time while the device is illuminated with laser pulses (λ = 2.5 µm).*

Now that we have shown that the coupling of the HgTe NC thin film to the photonic structure enables a broadband enhancement of the absorption (≈over 2500 cm^{-1} from 2 to 4 µm, see **Figure 4**d), it is essential to demonstrate the performance of this device for IR sensing. At low temperatures, the I-V curve appears to be superlinear, see **Figure 5**a. In the linear regime (below 0.1 V), the current drops as the temperature decreases. In the 300 K to 125 K range, the I-T curve can be fitted using Arrhenius law with an estimated activation energy of 125 meV. Under broadband illumination (*i.e.,* blackbody radiation at 980°C), the responsivity ranges from 400 to 700 $mA.W^{-1}$, depending on the temperature. The drop of responsivity below 120 K is connected to the thermal activation of the mobility resulting from hopping transport. While the carrier density decrease leads to a reduced dark current in this temperature range, carrier mobility drop may also affect the device's performance. Noise measurements show the dominant 1/f noise, see Figure S11. As the device is cooled down, the specific detectivity (*i.e.,* normalized signal to noise ratio) increases and reaches 2 x 10^{10} Jones

at 80 K for a 4 µm cut-off wavelength with light modulated at 1 kHz. The device's response time under the illumination of a 2.5 µm laser diode is estimated to be around 11 µs, see **Figure 5**c. Table 1 compares the performance of our device with state-of-the-art devices based on HgTe NCs presenting either multicolor sensing properties or designed light-matter coupling. In particular, our device presents one of the highest responsivities for MWIR (here, 4 µm cut-off wavelength) sensing devices thanks to its broadband enhancement of absorption. Regarding detectivity, it is only outperformed by a vertical geometry diode coupled to two resonators,[12] which, compared to our device, can be operated under zero bias and thus can reduce dark current.

Table 1 : Figures of merit for HgTe NCs sensors with multicolor or by design light-matter coupling

Material	**Device design**	**Spectral range/Cut-off wavelength**	**Responsivity (mA/W)**	**Time response**	**D* (Jones)**	**Operating Temperature (K)**	**References**
HgTe CdSe	Gate switchable photoresponse	Visible/SWIR 2.5 µm	0.17	-	-	300	[25]
HgTe	Coupling to plasmon	MWIR 4-5 µm	190	-	$1.52x10^{10}$	80	[10]
HgTe	Plasmon+ Fabry-Perot	MWIR 4.5-5 µm	1620	-	$4x10^{11}$	85	[12]
HgTe	Fabry-Perot	SWIR 2.2 µm	500	260 ns	$7.5x10^{10}$	300	[13]
HgTe	Dual band stacked photodiode	SWIR/MWIR 4-5 µm	400	2.5 µs	$3x10^{11}$	85	[26]
HgTe	Coupling to cavity to achieve 64 narrow bands	SWIR 2.08 µm	200	120 ns	10^{10}	295	[15]
HgTe	Coupling to plasmon	SWIR 2.3 µm	23	-	$3.2x10^{6}$	300	[11]
HgTe PbS	Guided mode resonator	SWIR and extended SWIR 3 µm	1000	-	10^{10}	200	[9]
HgTe	Bias shiftable photoresponse	MWIR 3.5-4 µm	60	5 µs	$8x10^{9}$	80	[14]
HgTe	3 resonances induced by GMR	SWIR 3 µm	-	14 µs	10^{12}	30	[27]

HgSe/HgTe	Intraband photodiode	MWIR/SWIR 5 µm	5	500 ns	$1.5x10^9$	80	[28]
HgTe	Multiresonant structure for board band enhancement of the absorption	MWIR 4 µm	>700	11 µs	$2x10^{10}$	80	**THIS WORK**

Conclusion

To summarize, we have demonstrated that broadband enhancement (over 2500 cm^{-1}) in light absorption can be obtained from a simple structure with a NC film coupled to a grating and a top metallic layer. This simple combination allows us to benefit from three different photonic modes: a double metal cavity mode, a surface plasmon mode in TM polarization, and a Fabry-Perot mode in TE. Both the TM and TE Fabry-Perot modes result from an impedance mismatch between the regions embedded between two metallic layers (*i.e.,* above the stripes) and those between the stripes. The obtained device enables sensing up to mid-wave infrared region (4 µm cut-off wavelength) with a high responsivity (>700 $mA.W^{-1}$) and a detectivity above 10^{10} Jones for 80 K operating temperature. Compared to previous works, our structure appears much easier to fabricate with a reduced number of fabrication steps, which is of utmost interest for the transfer of NC sensors to focal plane arrays.

Experimental section

Chemicals: Mercury chloride ($HgCl_2$, Sigma-Aldrich, 99%), tellurium powder (Te, Sigma-Aldrich, 99.99%), trioctylphosphine (TOP, Alfa, 90%), oleylamine (OLA, Acros, 80-90%), dodecanethiol (DDT, Sigma-Aldrich, 98%), 2-mercaptoethanol (MPOH, Merck, >99%), and N,N dimethylformamide (DMF, VWR), toluene (VWR, 99.8%) were used. All chemicals were used without further purification, except oleylamine that is centrifuged before use. **Mercury compounds are highly toxic. Handle them with special care.**

1 M TOP:Te precursor: Te powder (2.54 g) was mixed in 20 mL of TOP in a three-neck flask. The flask was kept under vacuum at room temperature for 5 mins, then the temperature was raised to 100 °C. Next, degassing of the flask was conducted for the next 20 minutes. The atmosphere was switched to nitrogen, and the temperature was raised to 275 °C. The solution was stirred until a clear orange color was obtained. The flask was cooled to room temperature, and the color changed to yellow. Finally, this solution was transferred to a nitrogen-filled glove box for storage.

HgTe NCs growth: In a 100mL three neck flask, 543 mg of $HgCl_2$ and 50 mL of oleylamine were degassed under vacuum at 110°C. Meanwhile, 2 mL of TOPTe (1M) were extracted from the glove box and mixed with 8 mL of oleylamine. After the flask atmosphere was switched to N_2 and the temperature stabilized at 95°C, the TOPTe solution was quickly injected. After 3 min, 10 mL of a mixture of DDT in toluene (10% of DDT) was injected and a water bath was used to decrease quickly the temperature. The content of the flask was splitted over 4 centrifuge tubes and MeOH was added. After centrifugation, the formed pellet was redispersed in one falcon with toluene. The solution was precipitated a second time using ethanol. Again, the formed pellet was redispersed in toluene. At this step the nanocrystals were centrifuged in pure toluene to get rid of the lamellar phase. The solid phase was discarded. The solution is filtered with a 0.2 µm filter and redispersed in 6 mL of toluene at a concentration of 50 $mg.mL^{-1}$.

HgTe ink preparation: 10 mg of $HgCl_2$, 2 mL of MPOH, and 18 mL of DMF are mixed to form an exchange solution. 0.25 mL of this exchange solution and 0.5 mL of DMF are added to 0.25 mL of HgTe NCs in toluene. Phase dissociation occurs when a few drops of hexane are added to the mixture: the dark bottom phase is where the NCs migrate while the top transparent phase can be removed with a plastic pipette. This washing step is repeated twice before adding a few mL of toluene. The mixture is then centrifuged at 6000 rpm for 4 minutes. The supernatant is discarded while the formed solid pellets of NCs can be re-dispersed in 100 µL of DMF to obtain the ink of HgTe. A few cycles of sonication – vortex – centrifugation can help promote particle dispersion.

Infrared Absorption spectroscopy: Absorbance spectra of NC solutions and NC inks are acquired with a Fisher IS50 Fourier transform infrared spectrometer. In the attenuated total reflection (ATR) mode, a small amount of NC solution (or NC ink) is dropped on the diamond cell and let to dry. The absorbance spectra are acquired over the range from 7500 cm^{-1} to 500 cm^{-1} with the resolution of 4 cm^{-1}, after averaging over 32 scans.

Responsivity under blackbody radiation: The device is placed inside the cryostat. A Femto DLPCA 200 amplifier is used to bias the photodetector, acquire and amplify the photocurrent signal. The amplified signal is then fed to an oscilloscope. The source is a Blackbody Omega BB-4A set at 980 ºC, placed 24 cm away from the sample. The incoming flux is chopped by an optical chopper with a frequency varied from 1 Hz to 1000 Hz. In front of the sample, a Ge window is used to filter out radiation at wavelengths shorter than 1.9 µm. Thus, the incident power onto the sample can be computed using the formula:

$$P(W) = \pi A_{det}.\sin^2\theta/2\,.\cos\varphi.\int_{1.9\mu m}^{\lambda_{cut-off}} \frac{2hc^2}{\lambda^5}\frac{1}{\exp\left(\frac{hc}{\lambda k T_{BB}}\right)-1}d\lambda$$

where A_{det} is the area of the photodetector, θ is the field of view, φ is the incident angle (typically assumed to be 0º), h is the Planck constant, c is the speed of light, k is Boltzmann constant, T_{BB} is the blackbody temperature equal to 980 ºC. $\lambda_{cut-off}$ is taken from the absorption edge of the material.

Noise measurement and detectivity: The device is biased with a Femto DLPCA 200 amplifier in noise measurements, while the signal is acquired on an SR780 spectrum analyzer. The noise spectra are typically acquired over a frequency range of 3 kHz, typically from 10 Hz to 3000 Hz. For one measurement, the final noise current density spectrum is obtained after averaging 100 scans. Detectivity values are extracted from $D^* = \frac{\mathcal{R}\sqrt{A}}{S_I}$, where $\mathcal{R}$ is the responsivity of the device, A is the device area (*i.e.*, 1.5 x 10^{-4} cm^2), and S_I is the measured noise current density.

Electromagnetic simulation: We use Comsol software to model the propagation of light in our plasmonic system. The model is constructed for one unit-cell of the resonator array, with Floquet

boundary conditions describing the periodicity. In the sapphire layer, a port condition is used to define the incident wave. On top of the sapphire, we define a perfectly matched layer to absorb all outgoing waves and prevent nonphysical reflections. The power density per unit volume dissipated in the NC film and metals is calculated from $P = -0.5\omega|F|^2 Im(\varepsilon)$, where F is the electric field, ω is the angular frequency of the incident wave, and $Im(\varepsilon)$ is the imaginary part of material permittivity. This quantity, divided by the incident power, gives the absorption per unit volume in the structure.

Electronic microscopy image on device: The TEM slice was prepared using a FEI Helios NanoLab600i dual beam SEM FIB fitted with an EasyLift micromanipulator for in situ lift-out. The ion column was operated at 30 kV for all the steps, except for final cleaning of the sample, for which tensions of 5 kV and 2 kV were used. The beam currents varied between 47 nA and 15 pA. The electron beam was used to deposit a 20 nm thick C layer over an area of 20 µm x 2 µm. The ion beam was then used to deposit a 3 µm thick layer Pt over the same area. The slice was partially cut out and a Pt needle was fixed. The sample was lifted out in situ and then attached to a copper support grid. Thinning of the sample could then be processed using a gradual cross-section cleaning milling pattern, with a final milling beam current of 80 pA. Finally, the 5 kV and 2 kV cleaning steps were carried out on each side The TEM images were performed with a JEOL 2100F TEM. The gun is a Schottky emitter used with a high voltage of 200kV. The slice was observed with a Gatan Rio16IS Camera in TEM mode. The EDS spectrum and mapping used a UltimMax windowless SDD from Oxord Inst. All the STEM images were done using HAADF STEM detector.

Supporting information

Supporting Information includes (*i*) electromagnetic design of the structure and associated input parameters, (*ii*) fabrication procedure and (*iii*) additional device characterization.

Conflict of interest

The authors declare no competing financial interest.

Keywords: infrared, photodetection, plasmon, cavity, resonances

ACKNOWLEDEGMENTS

We acknowledge Alexei Baranov (IES laboratory, University of Montpellier) for the 2.5 µm laser used for the measure of the time response of the device. The project is supported by ERC starting grant blackQD (grant n° 756225). We acknowledge the use of clean-room facilities from the “Centrale de Proximité Paris-Centre”. This work has been supported by the Region Ile-de-France in the framework of DIM Nano-K (grant dopQD). This work was supported by French state funds managed by the ANR within the Investissements d'Avenir programme under reference ANR-11-IDEX-0004-02, and more specifically within the framework of the Cluster of Excellence MATISSE and also by the grant IPER-Nano2 (ANR-18CE30-0023-01), Copin (ANR-19-CE24-0022), Frontal

(ANR-19-CE09-0017), Graskop (ANR-19-CE09-0026), NITQuantum (ANR-20-ASTR-0008-01), Bright (ANR-21-CE24-0012-02) and MixDferro (ANR-21-CE09-0029).

REFERENCES

[1] D. V Talapin, J. S. Lee, M. V Kovalenko, E. V Shevchenko, *Chem. Rev.* **2010**, *110*, 389.
[2] Y. Shirasaki, G. J. Supran, M. G. Bawendi, V. Bulović, *Nat. Photonics* **2013**, *7*, 13.
[3] G. H. Carey, A. L. Abdelhady, Z. Ning, S. M. Thon, O. M. Bakr, E. H. Sargent, *Chem. Rev.* **2015**, *115*, 12732.
[4] M. V Kovalenko, M. Scheele, D. V. Talapin, *Science.* **2009**, *324*, 1417.
[5] X. Tang, G. fu Wu, K. W. C. Lai, *J. Mater. Chem. C* **2017**, *5*, 362.
[6] A. Jagtap, B. Martinez, N. Goubet, A. Chu, C. Livache, C. Gréboval, J. Ramade, D. Amelot, P. Trousset, A. Triboulin, S. Ithurria, M. G. Silly, B. Dubertret, E. Lhuillier, *ACS Photonics* **2018**, *5*, 4569.
[7] P. Rastogi, A. Chu, C. Gréboval, J. Qu, U. N. Noumbé, S. S. Chee, M. Goyal, A. Khalili, X. Z. Xu, H. Cruguel, S. Ithurria, B. Gallas, J. F. Dayen, L. Dudy, M. G. Silly, G. Patriarche, A. Degiron, G. Vincent, E. Lhuillier, *Nano Lett.* **2020**, *20*, 3999.
[8] P. Rastogi, A. Chu, T. H. Dang, Y. Prado, C. Gréboval, J. Qu, C. Dabard, A. Khalili, E. Dandeu, B. Fix, X. Z. Xu, S. Ithurria, G. Vincent, B. Gallas, E. Lhuillier, *Adv. Opt. Mater.* **2021**, *9*, 2002066.
[9] A. Chu, C. Gréboval, N. Goubet, B. Martinez, C. Livache, J. Qu, P. Rastogi, F. A. Bresciani, Y. Prado, S. Suffit, S. Ithurria, G. Vincent, E. Lhuillier, *ACS Photonics* **2019**, *6*, 2553.
[10] Y. Yifat, M. Ackerman, P. Guyot-Sionnest, *Appl. Phys. Lett.* **2017**, *110*, 041106.
[11] B. Zhu, M. Chen, Q. Zhu, G. Zhou, N. M. Abdelazim, W. Zhou, S. V Kershaw, A. L. Rogach, N. Zhao, H. K. Tsang, *Adv. Mater. Technol.* **2019**, *4*, 1900354.
[12] X. Tang, M. M. Ackerman, P. Guyot-Sionnest, *ACS Nano* **2018**, *12*, 7362.
[13] X. Tang, M. M. Ackerman, G. Shen, P. Guyot-Sionnest, *Small* **2019**, *15*, 1804920.
[14] T. H. Dang, A. Vasanelli, Y. Todorov, C. Sirtori, Y. Prado, A. Chu, C. Gréboval, A. Khalili, H. Cruguel, C. Delerue, G. Vincent, E. Lhuillier, *Nano Lett.* **2021**, *21*, 6671.
[15] X. Tang, M. M. Ackerman, P. Guyot-Sionnest, *Laser Photonics Rev.* **2019**, *13*, 1900165.
[16] H. L. Chen, A. Cattoni, R. De Lépinau, A. W. Walker, O. Höhn, D. Lackner, G. Siefer, M. Faustini, N. Vandamme, J. Goffard, B. Behaghel, C. Dupuis, N. Bardou, F. Dimroth, S. Collin, *Nat. Energy* **2019**, *4*, 761.
[17] Y. Todorov, L. Tosetto, J. Teissier, A. M. Andrews, P. Klang, R. Colombelli, I. Sagnes, G. Strasser, C. Sirtori, *Opt. Express* **2010**, *18*, 13886.
[18] P. Jouy, Y. Todorov, A. Vasanelli, R. Colombelli, I. Sagnes, C. Sirtori, *Appl. Phys. Lett.* **2011**, *98*, 021105.
[19] C. Gréboval, A. Chu, N. Goubet, C. Livache, S. Ithurria, E. Lhuillier, *Chem. Rev.* **2021**, *121*, 3627.
[20] S. Keuleyan, E. Lhuillier, P. Guyot-Sionnest, *J. Am. Chem. Soc.* **2011**, *133*, 16422.
[21] S.-S. Chee, C. Gréboval, D. V. Magalhaes, J. Ramade, A. Chu, J. Qu, P. Rastogi, A. Khalili, T. H. Dang, C. Dabard, Y. Prado, G. Patriarche, J. Chaste, M. Rosticher, S. Bals, C. Delerue, E. Lhuillier, *Nano Lett.* **2021**, *21*, 4145.
[22] B. Martinez, J. Ramade, C. Livache, N. Goubet, A. Chu, C. Gréboval, J. Qu, W. L. Watkins, L. Becerra, E. Dandeu, J. L. Fave, C. Méthivier, E. Lacaze, E. Lhuillier, *Adv. Opt. Mater.* **2019**, *7*, 1900348.
[23] X. Lan, M. Chen, M. H. Hudson, V. Kamysbayev, Y. Wang, P. Guyot-Sionnest, D. V. Talapin, *Nat. Mater.* **2020**, *19*, 323.
[24] M. Chen, X. Lan, X. Tang, Y. Wang, M. H. Hudson, D. V. Talapin, P. Guyot-Sionnest, *ACS*

Photonics **2019**, *6*, 2358.
[25] E. Lhuillier, A. Robin, S. Ithurria, H. Aubin, B. Dubertret, *Nano Lett.* **2014**, *14*, 2715.
[26] X. Tang, M. M. Ackerman, M. Chen, P. Guyot-Sionnest, *Nat. Photonics* **2019**, *13*, 277.
[27] C. Gréboval, A. Chu, D. V. Magalhaes, J. Ramade, J. Qu, P. Rastogi, A. Khalili, S. S. Chee, H. Aubin, G. Vincent, S. Bals, C. Delerue, E. Lhuillier, *ACS Photonics* **2021**, *8*, 259.
[28] C. Livache, B. Martinez, N. Goubet, C. Gréboval, J. Qu, A. Chu, S. Royer, S. Ithurria, M. G. Silly, B. Dubertret, E. Lhuillier, *Nat. Commun.* **2019**, *10*, 2125.